# Direct Synthesis of $H_2O_2$ on PdZn Nanoparticles: The Impact of Electronic Modifications and Heterogeneity of Active Sites

Neil M. Wilson[1], Johanna Schröder[2], Pranjali Priyadarshini[1], Daniel T. Bregante[1], Sebastian Kunz[2], and David W. Flaherty[1,*]

Supporting Information

[1]Department of Chemical and Biomolecular Engineering
University of Illinois Urbana-Champaign, Urbana, IL 61801

[2]Institute of Applied and Physical Chemistry
University of Bremen, Bremen, Germany

*Corresponding Author
Phone: (217) 244-2816
Email: dwflhrty@illinois.edu

**S1. Evidence for the Absence of Mass Transport Limitations**

The following procedure for ensuring that there are no mass transport restrictions has been described previously [1]. Briefly, the Madon-Boudart experimental criterion for the absence of mass transport restrictions [2] is satisfied on 0.05 wt. % Pd supported on Davisil 646 $SiO_2$ [3]. Therefore, the diffusion modulus (φ) [4] for that Pd-$SiO_2$ catalyst is much less than one:

$$\varphi = R\sqrt{\frac{k}{D}} \ll 1 \qquad \text{(S1)}$$

where *R* is the radius of the silica particles, *k* is the rate constant for $H_2$ consumption, and *D* is the diffusion constant of $H_2$ and $O_2$ through the silica pores. The value of *k* can be quantified by the rate of $H_2$ consumption per unit volume of catalyst ($\frac{dn_v}{dt}$)[4]:

$$\varphi = \frac{R^2}{D}\frac{1}{c}\frac{dn_v}{dt} \qquad \text{(S2)}$$

The same silica was used for the $PdZn_x$ catalysts used here (i.e., no change in *R* and *C*), and so at the same $H_2$ and $O_2$ pressure (i.e., no change *c*), the ratio of φ for Pd ($\varphi_{Pd}$) and $PdZn_x$ ($\varphi_{PdZn_x}$) (Φ) becomes:

$$\Phi = \frac{\varphi_{Pd}}{\varphi_{PdZn_x}} = \frac{\frac{dn_{v,Pd}}{dt}}{\frac{dn_{v,PdZn_x}}{dt}} \qquad \text{(S3)}$$

where $\frac{dn_{v,x}}{dt}$ is the rate of $H_2$ consumption per unit volume on catalyst *x*. In the absence of mass transport restrictions on $PdZn_x$ catalysts, the value of Φ should be greater than or equal to one. At standard conditions selected for these comparisons (55 kPa $H_2$, 60 kPa $O_2$ and 273 K), values of Φ are 5.1 $\pm$ 0.8 on $PdZn_{1.5}$, 1.5 $\pm$ 0.2 on $PdZn_6$, and 6.2 $\pm$ 1.1 on $PdZn_{30}$, indicating that rates were measured in the absence of mass transport limitations on all $PdZn_x$ catalysts.

## S2. TEM Images and Size Distributions for High Metal Loading Catalysts

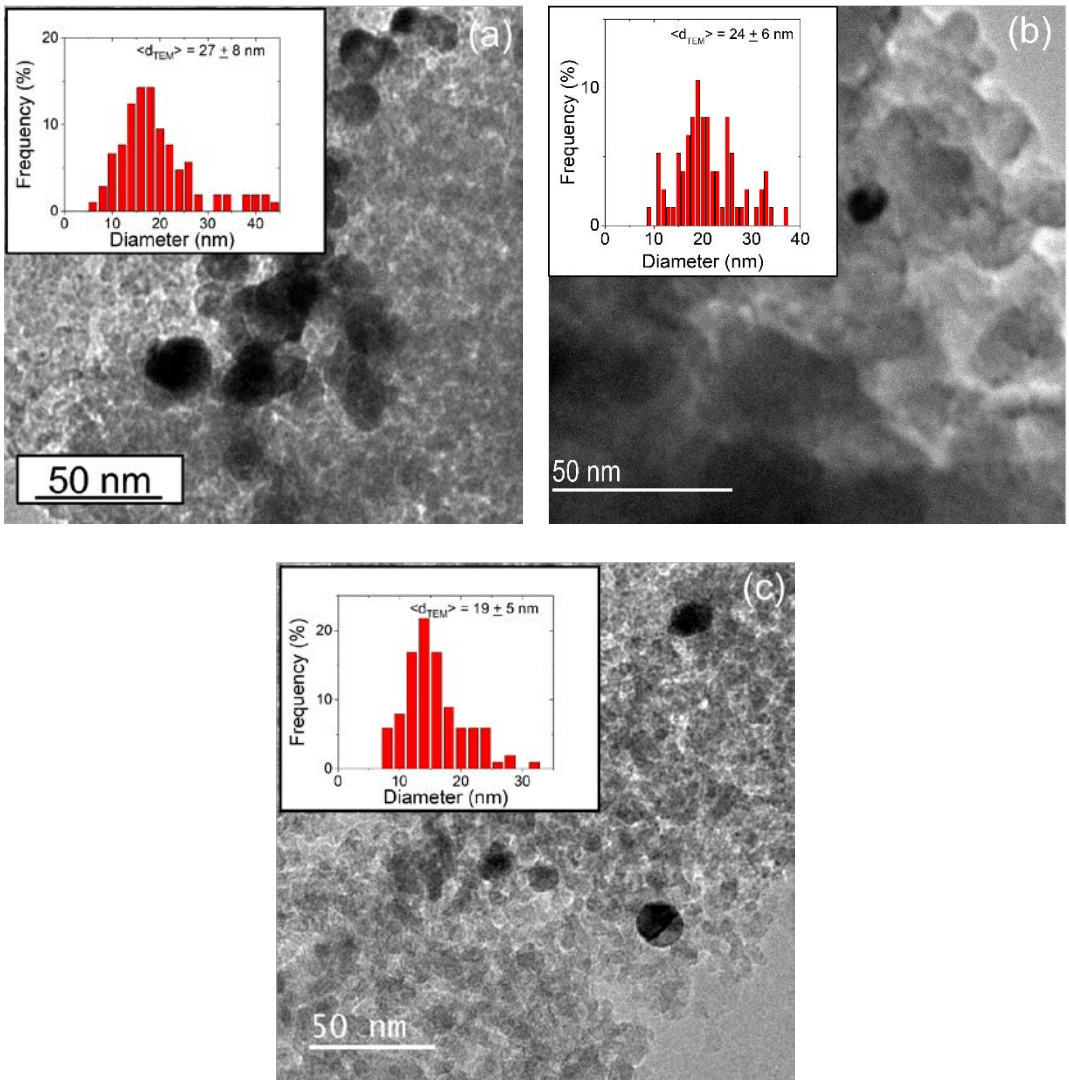


Figure S1. Representative TEM images of high metal loading (0.19-1.4 wt. % Pd), silica supported (a) ω-Pd, (b) ω-$Pd_1Zn_4$, and (c) ω-$Pd_1Zn_{20}$ catalysts with their corresponding size distribution and $<d_{TEM}>$ value as inset. More than 100 nanoparticles were counted for each size distribution.

**S3. Selected Area Electron Diffractograms and Brightness Intensity Profiles**

Select nanoparticles were characterized by both transmission electron microscopy (TEM) and selected area electron diffraction (SAED). Intensity profiles were determined in ImageJ and multiple intensity profiles were collected from individual diffractograms, which were averaged to yield a single intensity profile representative of that diffractogram. Below, are TEM images and their corresponding SAED diffractograms and diffractogram brightness intensity profiles for Pd (Figures S2), $PdZn_{1.5}$ (Figure S3), and $PdZn_6$ (Figure S4) nanoparticles, which are intended to demonstrate that coexistence of both face-centered cubic (fcc) Pd and $\beta_1$-$Pd_1Zn_1$ nanoparticles (for the $PdZn_{1.5}$ and $PdZn_6$ materials) within these samples. Similar characterization of $PdZn_{30}$ (not shown) gave only evidence for $\beta_1$-$Pd_1Zn_1$ nanoparticles.

Note, calculations considering the camera length of the TEM show that reflections in the range of 4.6-5.1 and 9.3-10.1 $nm^{-1}$ are indicative of the (111) and (200) reflections of fcc Pd and $PdZn_y$, while those in the range of 4.3-4.4 and 7.7-8.4 $nm^{-1}$ arise from diffraction from (111) and the $\beta_1$-$Pd_1Zn_1$ phase .

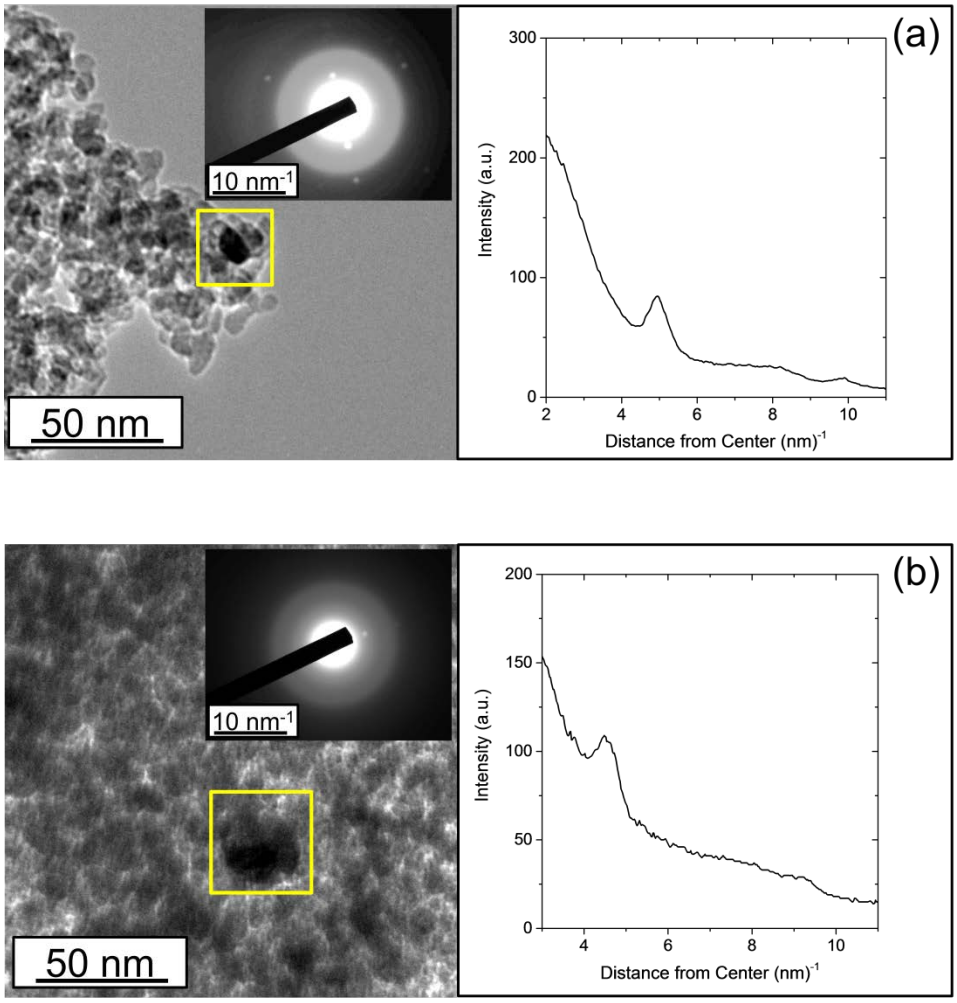


Figure S2. TEM images (left) of two separate Pd nanoparticles (highlighted by yellow box) and their corresponding SAED diffractograms (inset) and brightness intensity profiles (right). The intensity profiles show the presence of diffraction features indicative of the face centered cubic phase of Pd.

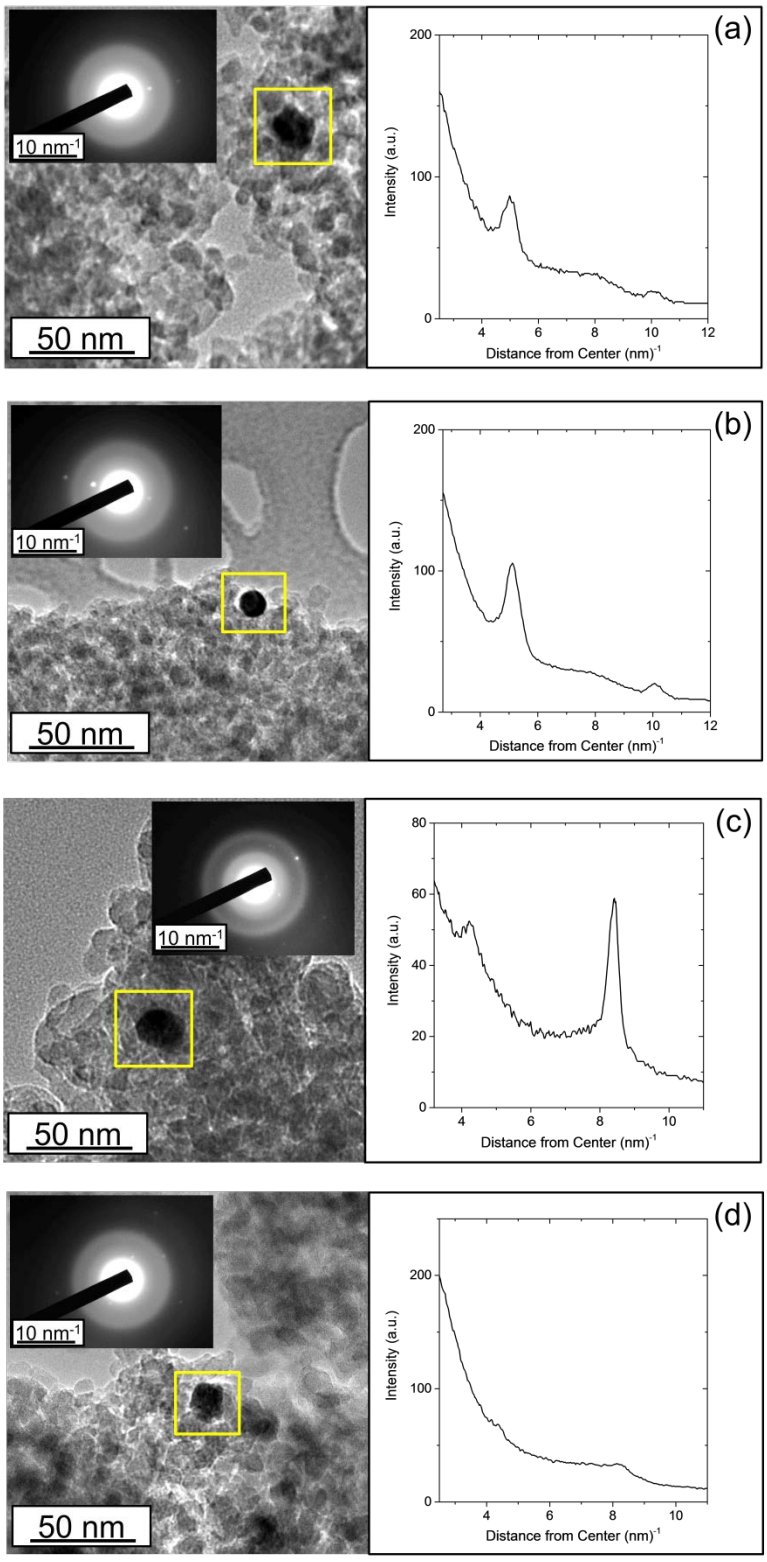


Figure S3. TEM images (left) of four separate $PdZn_{1.5}$ nanoparticles (highlighted by yellow box) and their corresponding SAED diffractograms (inset) and brightness intensity profiles (right). Intensity profiles show the presence of face centered cubic Pd, (a) and (b); and also nanoparticles that exist as the $\beta_1$-$Pd_1Zn_1$ phase, (c) and (d).

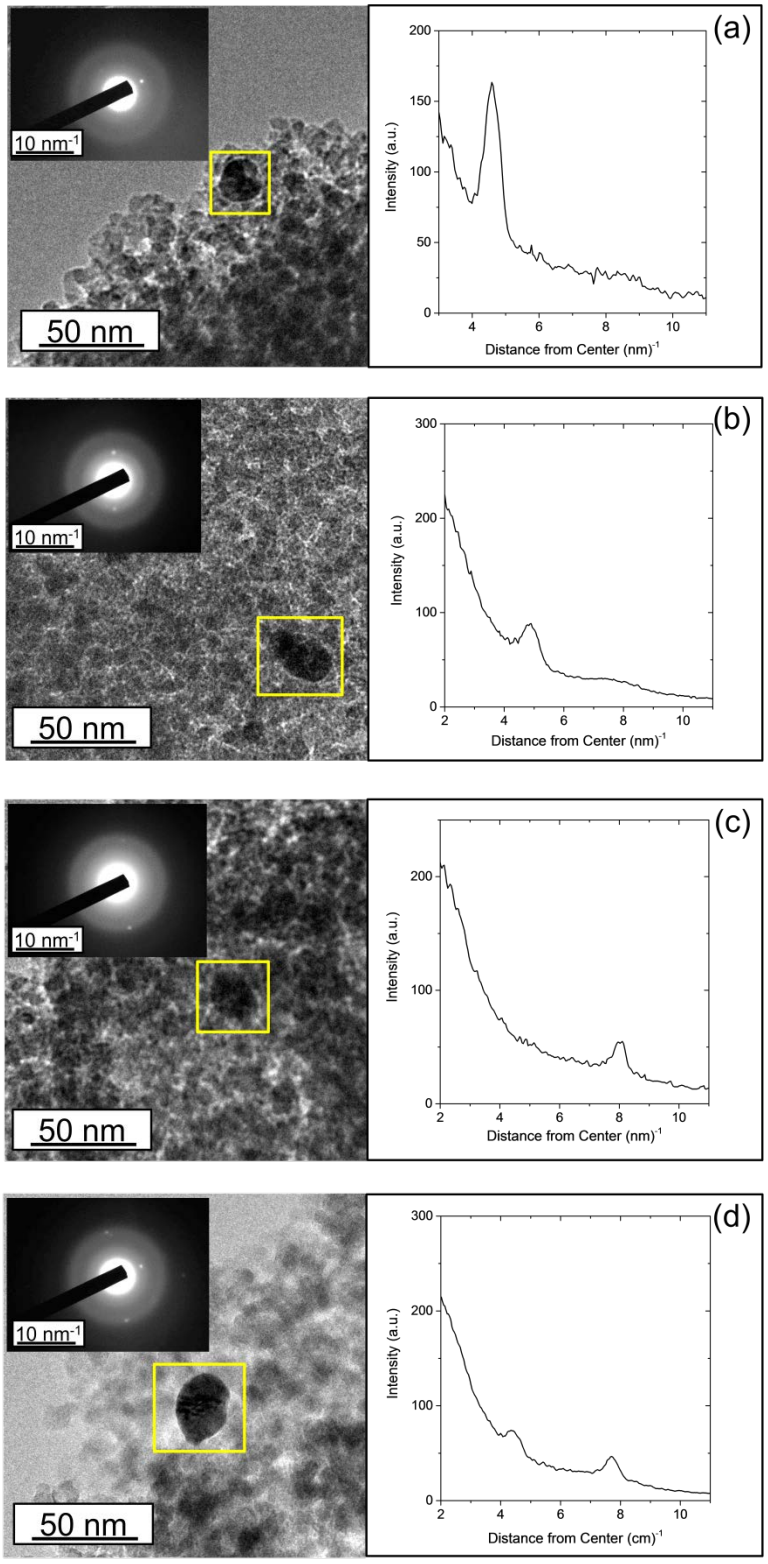


Figure S4. TEM images (left) of four separate $PdZn_6$ nanoparticles (highlighted by yellow box) and their corresponding SAED diffractograms (inset) and brightness intensity profiles (right). The intensity profiles show the presence of both face centered cubic Pd, (a) and (b); and $\beta_1$-$Pd_1Zn_1$ nanoparticles, (c) and (d).

## S4. STEM-EDX Mapping of $PdZn_{30}$

$PdZn_{30}$ nanoparticles were also characterized by dark-field scanning transmission electron microscopy (STEM; JEOL 2010F EF-FEG) in combination with energy dispersive X-ray spectroscopy (EDX; Oxford Instruments, 6498) to determine if Pd and Zn co-existed within clusters and to determine if excess Zn was present on the support. Pd and Zn were found to co-exist in the same cluster as seen from the EDX map in Figure S5a.We were not able to detect excess Zn on the support as seen from additional mapping of random location on the support (Figure S5b-e). These methods show that Pd and Zn coexist within individual nanoparticles (see Figure S5a) but also show extremely small quantities (near the detection limit, and undetectable by XRD) of Pd and Zn exist on the support as monometallic oligomers (< 1 nm in diameter) despite the colloidal approach used to synthesize these catalysts (Figures S5b – S5e).

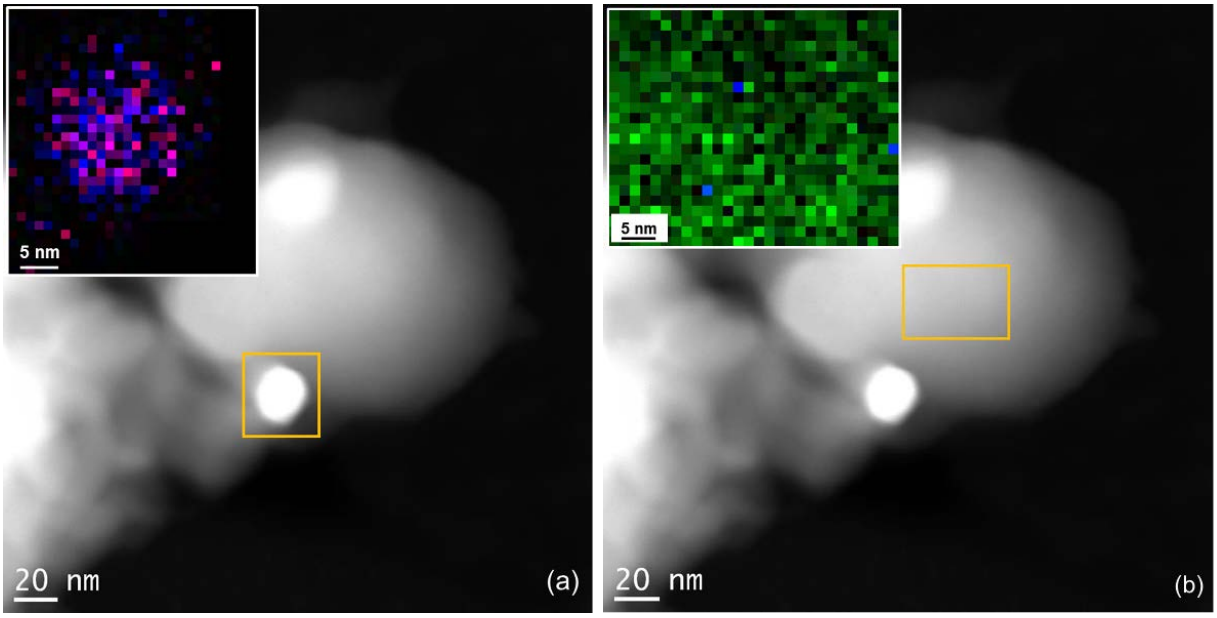

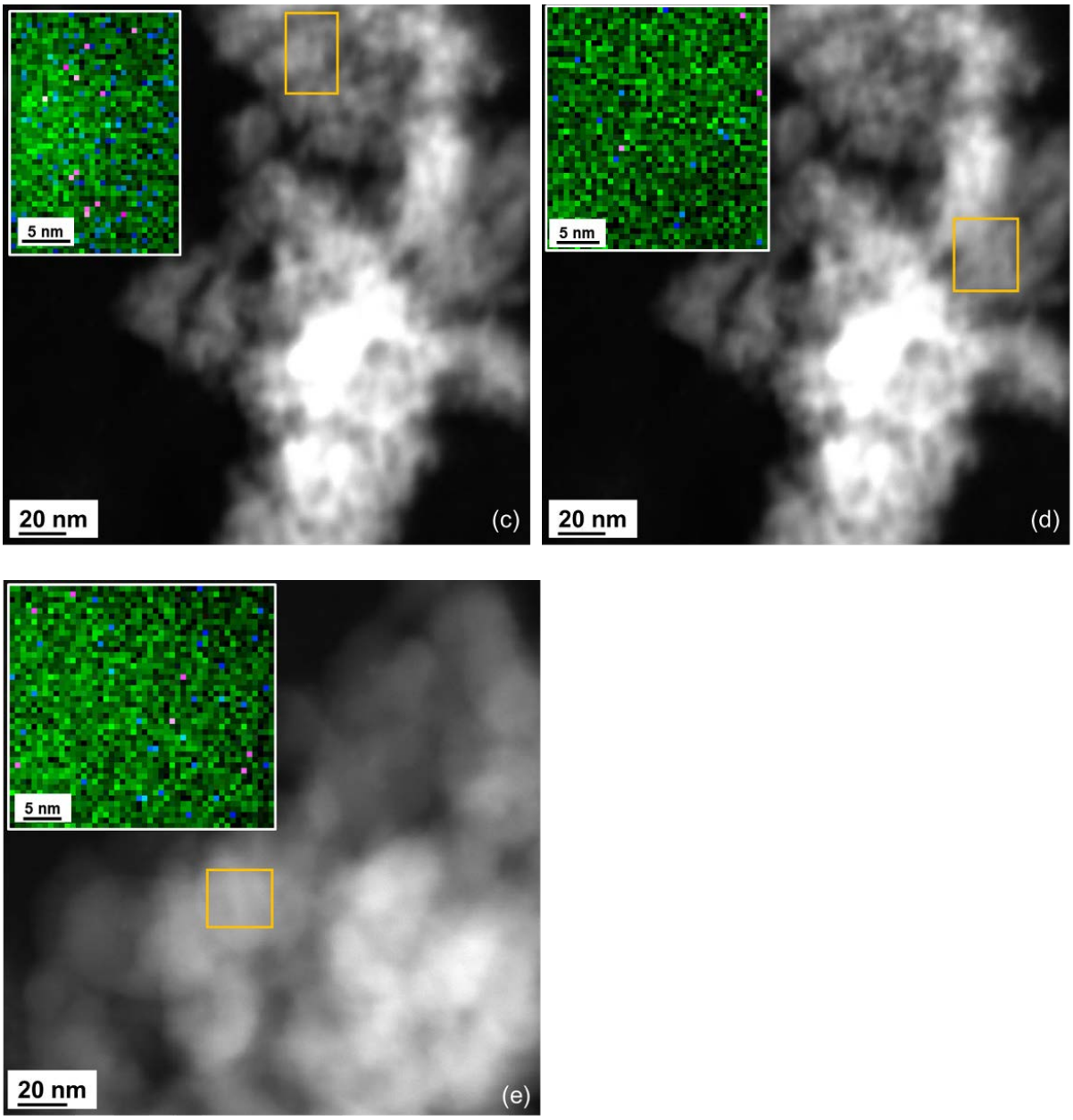


Figure S5. STEM images and EDX maps for the $PdZn_{30}$ material. (a) STEM image of a single nanoparticle (yellow box) with EDX map of Pd (blue) and Zn (pink) (inset). (b-e) STEM images of randomly selected locations of the $SiO_2$ support with EDX maps of Si (green), Pd (blue) and Zn (pink).

## S5. Rates and Selectivity on $PdZn_x$ Catalysts over Long Times on Stream

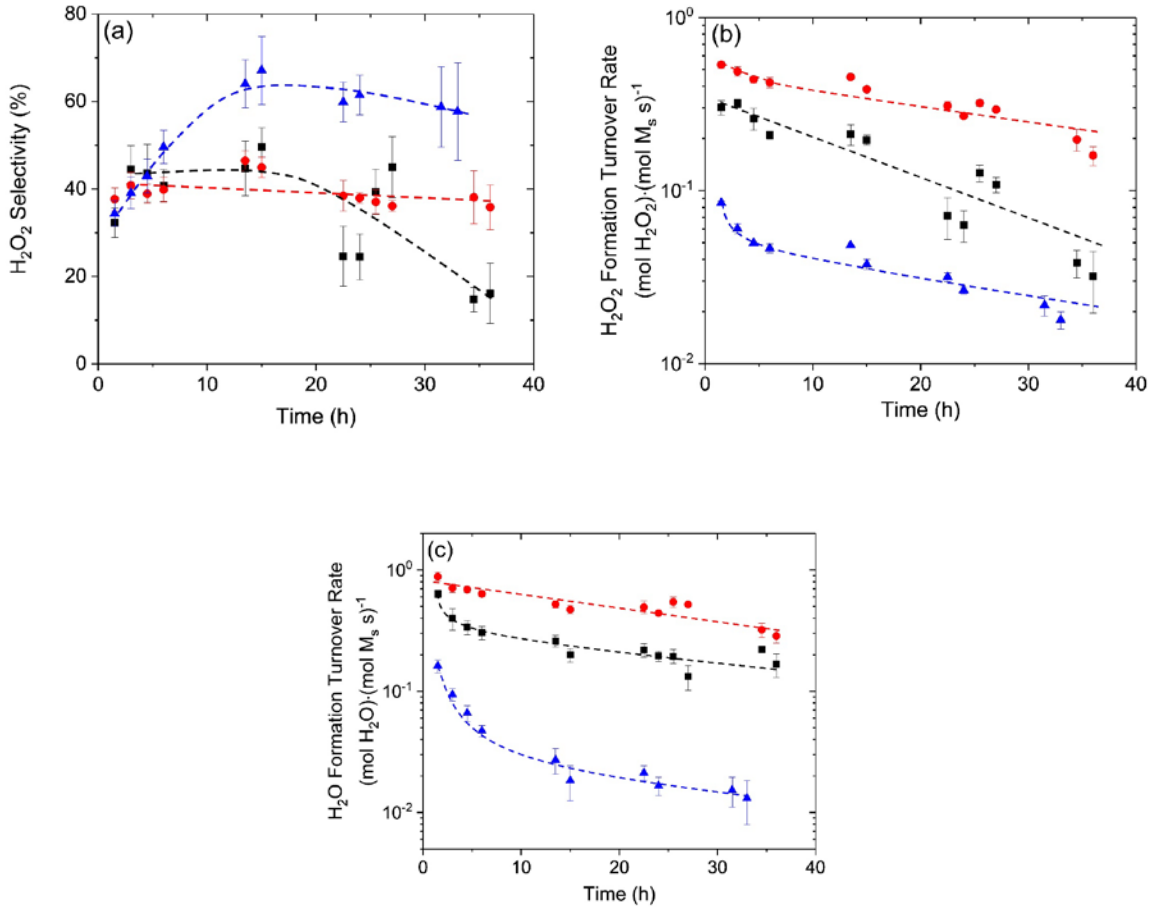


Figure S6. (a) $H_2O_2$ selectivity and (b) $H_2O_2$ and (c) $H_2O$ formation turnover rates as a function of time on $PdZn_{1.5}$ (■), $PdZn_6$ (●), and $PdZn_{30}$ (▲) catalysts (55 kPa $H_2$, 60 kPa $O_2$, 273 K, 30 $cm^3$ $min^{-1}$ 20% v/v methanol). Dashed lines are intended to guide the eye.

**S6. Derivation of the Proton-Electron Transfer Mechanism**

The derivation of this mechanism and the detailed assumptions made have been described previously [3, 5]. Scheme S1 shows the complete proposed mechanism for both $H_2O_2$ and $H_2O$ formation.

$$H_2 + 2* \underset{k_{-1}}{\overset{k_1}{\rightleftharpoons}} 2H* \quad (1)$$

$$H* \underset{k_{-2}}{\overset{k_2}{\rightleftharpoons}} H^+ + e^- + * \quad (2)$$

$$O_2 + ** \underset{k_{-3}}{\overset{k_3}{\rightleftharpoons}} O_2** \quad (3)$$

$$O_2** + H^+ + e^- \underset{k_{-4}}{\overset{k_4}{\rightleftharpoons}} OOH** \quad (4)$$

$$OOH** + H^+ + e^- \xrightarrow{k_5} H_2O_2** \quad (5)$$

$$H_2O_2** \underset{k_{-6}}{\overset{k_6}{\rightleftharpoons}} H_2O_2 + ** \quad (6)$$

$$O_2** \xrightarrow{k_7} 2O* \quad (7)$$

$$OOH** \xrightarrow{k_8} OH* + O* \quad (8)$$

$$O* + H* \xrightarrow{k_9} OH* + * \quad (9)$$

$$OH* + H* \xrightarrow{k_{10}} H_2O* + * \quad (10)$$

$$H_2O* \underset{k_{-11}}{\overset{k_{11}}{\rightleftharpoons}} H_2O + * \quad (11)$$

$$H_2O_2** \xrightarrow{k_{12}} 2OH* \quad (12)$$

Scheme S1. Proposed series of elementary steps for $H_2O_2$ and $H_2O$ formation during direct synthesis on supported Pd clusters. Here, * denotes an empty site, X* represents an adsorbate bound to a single Pd atom, X** signifies an intermediate adsorbed in an $\eta^2$ (i.e., multidentate) configuration, $\rightleftharpoons$ indicates that an elementary step is quasi-equilibrated, and $k_x$ is the rate constant for elementary step x.

It can be inferred from Scheme S1 that the rate of $H_2O_2$ formation ($r_{H_2O_2}$) increases with the number of OOH** surface intermediates ([$OOH$**]) and the number of available protons ([$H^+$]) and electrons ([$e^-$]) (Scheme S1, step 5) but decreases with the number of $H_2O_2$** surface intermediates ([$H_2O_2$**]) by secondary decomposition. These relationships can be described with the following rate expression:

$$r_{H_2O_2} = k_5[OOH\ **][H^+][e^-] - k_{12}[H_2O_2\ **] \qquad \text{(S5)}$$

where $k_x$ is the rate constant for elementary step $x$. After applying the pseudo steady-state hypothesis to the reactive intermediates in equation S5, the rate expression can be represented by $H_2$ and $O_2$ partial pressures ($(H_2)$ and $(O_2)$, respectively) and the solvent $H_2O_2$ concentration ($(H_2O_2)$):

$$r_{H_2O_2} = \left(k_5 K_4 K_3 {K_2}^2 K_1 (O_2)(H_2) - \frac{k_{12}}{K_6}(H_2O_2)\right)[**] \qquad \text{(S6)}$$

where $K_x$ is the equilibrium constant for elementary step $x$ and [**] is the number of unoccupied active sites. Computational investigations of surface bound $O_2$ and OOH intermediates indicate these species likely bind to two or more neighboring Pd atoms in $\eta^2$ and bent $\eta^1$ configurations [6-10], where one O-atom may reside in a three-fold hollow while the other coordinates to a two-fold or atop site. Consequently, we denote these species as $O_2$** or OOH** to reflect the multidentate coordination of these intermediates to ensembles of metal atoms. Next, an overall site balance is performed:

$$[L] = [**] + [O_2\ **] + [OOH\ **] + [H_2O_2\ **] \qquad \text{(S7)}$$

where $[L]$ is the total number of sites and $[O_2**]$ is the number of $O_2$** intermediates. Notably, this site balance does not reflect the presence of chemisorbed H* atoms, because the kinetic measurements reported here as well in our previous publications do not provide clear evidence for the inhibition of rates by $(H_2)$ and therefore do not reflect consequential coverages of H* atoms.

It was assumed that steps 1-4 and 6 are in quasi-equilibrium, and can therefore be expressed by equilibrium constants:

$$K_1 = \frac{[H*]^2}{(H_2)[*]^2} \qquad \text{(S8)}$$

for step 1:

$$K_2 = \frac{[H^+][e^-][*]}{[H*]} \qquad \text{(S9)}$$

for step 2:

$$K_3 = \frac{[O_2{**}]}{(O_2)[{**}]} \quad \text{(S10)}$$

for step 3:

$$K_4 = \frac{[OOH{**}]}{[O_2{**}][H^+][e^-]} \quad \text{(S11)}$$

for step 4 and:

$$K_6 = \frac{(H_2O_2)[{**}]}{[H_2O_2{**}]} \quad \text{(S12)}$$

for step 6. Equations S8-S12 can then be used to derive terms for [$O_2$**]:

$$[O_2\ {**}] = K_3(O_2)[{**}] \quad \text{(S13)}$$

for [*OOH***]:

$$[OOH\ {**}] = K_4K_3K_2K_1^{\frac{1}{2}}(O_2)(H_2)^{\frac{1}{2}}[{**}] \quad \text{(S14)}$$

and for [$H_2O_2$**]:

$$[H_2O_2\ {**}] = \frac{1}{K_6}(H_2O_2)[{**}] \quad \text{(S15)}$$

which are then substituted into equation S7:

$$[L] = [{**}] + K_3(O_2)[{**}] + K_4K_3K_2K_1^{\frac{1}{2}}(O_2)(H_2)^{\frac{1}{2}}[{**}] + \frac{1}{K_6}(H_2O_2)[{**}] \quad \text{(S16)}$$

Solving equation S16 for [**] and substituting into equation S6 yields the rate expression for $H_2O_2$ formation by a proton-electron transfer mechanism:

$$\frac{r_{H_2O_2}}{[L]} = \frac{k_5K_4K_3K_2{}^2K_1(H_2)(O_2) - \frac{k_{12}}{K_6}(H_2O_2)}{1 + K_3(O_2) + K_4K_3K_2K_1^{\frac{1}{2}}(H_2)^{\frac{1}{2}}(O_2) + \frac{1}{K_6}(H_2O_2)} \quad \text{(S17)}$$

It has been shown previously [5] that at the high liquid flow rates implemented in this study (30 $cm^3$ $min^{-1}$), the concentration of $H_2O_2$ is minimized and the $\frac{k_{12}}{K_6}(H_2O_2)$ term can be considered negligible, yielding the following simplified rate expression:

$$\frac{r_{H_2O_2}}{[L]} = \frac{k_5 K_4 K_3 {K_2}^2 K_1 (H_2)(O_2)}{1+K_3(O_2)+K_4 K_3 K_2 K_1^{\frac{1}{2}} (H_2)^{\frac{1}{2}} (O_2)+\frac{1}{K_6}(H_2O_2)} \quad \text{(S18)}$$

The rate of $H_2O$ formation ($r_{H_2O}$) can be described by the summation of rates of O-O bond scission in $O_2$** (Scheme S1, step 7), OOH** (Scheme S1, step 8), and $H_2O_2$** (Scheme S1, step 12):

$$r_{H_2O} = k_7[O_2\ **] + k_8[OOH\ **] + k_{12}[H_2O_2\ **] \quad \text{(S19)}$$

By substituting equations S13-S15 into equation S19, the $H_2O$ formation rate becomes:

$$r_{H_2O} = k_7 K_3 (O_2)[**] + k_8 K_4 K_3 K_2 K_1^{\frac{1}{2}} (O_2)(H_2)^{\frac{1}{2}}[**] + k_{12}\frac{1}{K_6}(H_2O_2)[**] \quad \text{(S20)}$$

Substitution of the site balance (equation S16) into equation S20 yields:

$$\frac{r_{H_2O}}{[L]} = \frac{k_7 K_3 (O_2)+k_8 K_4 K_3 K_2 K_1^{\frac{1}{2}} (H_2)^{\frac{1}{2}} (O_2)+\frac{k_{12}}{K_6}(H_2O_2)}{1+K_3(O_2)+K_4 K_3 K_2 K_1^{\frac{1}{2}} (H_2)^{\frac{1}{2}} (O_2)+\frac{1}{K_6}(H_2O_2)} \quad \text{(S21)}$$

Calculated energy barriers [6, 8] suggest that primary $H_2O$ formation rates occur by breaking the O-O bond in OOH** intermediates, allowing equation S21 to be simplified to:

$$\frac{r_{H_2O}}{[L]} = \frac{k_8 K_4 K_3 K_2 K_1^{\frac{1}{2}} (H_2)^{\frac{1}{2}} (O_2)+\frac{k_{12}}{K_6}(H_2O_2)}{1+K_3(O_2)+K_4 K_3 K_2 K_1^{\frac{1}{2}} (H_2)^{\frac{1}{2}} (O_2)+\frac{1}{K_6}(H_2O_2)} \quad \text{(S22)}$$

Again, at 30 $cm^3\ min^{-1}$ liquid flow rate, the $\frac{k_{12}}{K_6}(H_2O_2)$ term can be considered negligible and the rate of $H_2O$ formation becomes:

$$\frac{r_{H_2O}}{[L]} = \frac{k_8 K_4 K_3 K_2 K_1^{\frac{1}{2}} (H_2)^{\frac{1}{2}} (O_2)}{1+K_3(O_2)+K_4 K_3 K_2 K_1^{\frac{1}{2}} (H_2)^{\frac{1}{2}} (O_2)+\frac{1}{K_6}(H_2O_2)} \quad \text{(S23)}$$

## S7. Calculation of Activation Enthalpies for $H_2O$ Formation

Like $H_2O_2$ formation (equation 8), the transition state for $H_2O$ formation is in equilibrium with reactant species which are in equilibrium also with gaseous $H_2$ ($H_2(g)$) and adsorbed $O_2$ ($O_2$**). This allows for the number of transition state species for $H_2O$ formation ($O-OH\ **^{\ddagger}$) to be expressed using an equilibrium constant ($K^{\ddagger}{}_{H_2O}$):

$$O_2\ ** + \frac{1}{2}H_2(g) \overset{K^{\ddagger}{}_{H_2O}}{\longleftrightarrow} O-OH\ **^{\ddagger} \qquad \text{(S24)}$$

Conventions of transition state theory and the equilibrium described by equation S24 allow for the $H_2O$ formation turnover rate ($\frac{r_{H_2O}}{[L]}$) to be described by $K^{\ddagger}{}_{H_2O}$:

$$\frac{r_{H_2O}}{[L]} = \frac{k_B T}{h} K^{\ddagger}{}_{H_2O} (H_2)^{\frac{1}{2}} \qquad \text{(S25)}$$

where $T$ is the temperature in Kelvin, and $h$ and $k_B$ are Planck's and Boltzmann's constants, respectively. Changes in free energy ($\Delta G^{\ddagger}$) were then calculated using:

$$K_x{}^{\ddagger} = e^{-\Delta G_x{}^{\ddagger}/RT} \qquad \text{(S26)}$$

where $K_x{}^{\ddagger}$ is the equilibrium constant for product $x$ and $R$ is the ideal gas constant. Activation enthalpies ($\Delta H_x{}^{\ddagger}$) and entropies ($\Delta S_x{}^{\ddagger}$) for product $x$ were then determined from equation S26 using $\Delta G^{\ddagger}=\Delta H^{\ddagger}-T\Delta S^{\ddagger}$:

$$K_x{}^{\ddagger} = e^{-\Delta H_x{}^{\ddagger}/RT} \cdot e^{\Delta S_x{}^{\ddagger}/R} \qquad \text{(S27)}$$

## References


[1] N.M. Wilson, Y.-T. Pan, Y.-T. Shao, J.-M. Zuo, H. Yang, D.W. Flaherty, Direct Synthesis of $H_2O_2$ on AgPt Octahedra: the Importance of Pt-Ag Interactions for High $H_2O_2$ Selectivities, ACS Catal., 8 (2018) 2880-2889.

[2] R.J. Madon, M. Boudart, Experimental Criterion for the Absence of Artifacts in the Measurement of Rates of Heterogeneous Catalytic Reactions, Ind. Eng. Chem. Fundam., 21 (1982) 438-447.

[3] N.M. Wilson, D.W. Flaherty, Mechanism for the Direct Synthesis of $H_2O_2$ on Pd Clusters: Heterolytic Reaction Pathways at the Liquid-Solid Interface, J. Am. Chem. Soc., 138 (2016) 574-586.

[4] P.B. Weisz, C.D. Prater, Interpretation of Measurements in Experimental Catalysis, Adv. Catal., 6 (1954) 143-196.

[5] N.M. Wilson, P. Priyadarshini, S. Kunz, D.W. Flaherty, Direct Synthesis of $H_2O_2$ on Pd and $Au_xPd_1$ Clusters: Understanding the Effects of Alloying Pd with Au, J. Catal., 357 (2018) 163-175.

[6] A. Plauck, E.E. Strangland, J.A. Dumesic, M. Mavrikakis, Active Sites and Mechanisms for $H_2O_2$ Decomposition over Pd Catalysts, Proc. Natl. Acad. Sci., 113 (2016) E1973-E1982.

[7] C.A. Farberow, A. Godinez-Garcia, G. Peng, J.F. Perez-Robles, O. Solorza-Feria, M. Mavrikakis, Mechanistic Studies of Oxygen Reduction by Hydrogen on PdAg(110), ACS Catalysis, 3 (2013) 1622-1632.

[8] D.C. Ford, A.U. Nilekar, Y. Xu, M. Mavrikakis, Partial and Complete Reduction of $O_2$ by Hydrogen on Transition Metal Surfaces, Surf. Sci., 604 (2010) 1565-1575.

[9] R. Todorovic, R.J. Meyer, A Comparative Density Functional Theory Study of the Direct Synthesis of $H_2O_2$ on Pd, Pt and Au surfaces, Catalysis Today, 160 (2011) 242-248.

[10] W.-Y. Yu, L. Zhang, G.M. Mullen, G. Henkelman, C.B. Mullins, Oxygen Activation and Reaction on Pd−Au Bimetallic Surfaces, Journal of Physical Chemistry C, 119 (2015) 11754-11762.